

# Attractor metadynamics in terms of target points in slow–fast systems: adiabatic vs. symmetry protected flow in a recurrent neural network

Hendrik Wernecke,<sup>1</sup> Bulcsú Sándor,<sup>2</sup> and Claudius Gros<sup>1,\*</sup>

<sup>1</sup>*Institute for Theoretical Physics, Goethe University Frankfurt, Germany*

<sup>2</sup>*Department of Physics, Babeş-Bolyai University, Cluj-Napoca, Romania*

(Dated: May 3, 2021)

In dynamical systems with distinct time scales the time evolution in phase space may be influenced strongly by the fixed points of the fast subsystem. Orbits then typically follow these points, performing in addition rapid transitions between distinct branches on the time scale of the fast variables. As the branches guide the dynamics of a system along the manifold of former fixed points, they are considered transiently attracting states and the intermittent transitions between branches correspond to state switching within transient–state dynamics.

A full characterization of the set of former fixed points, the critical manifold, tends to be difficult in high–dimensional dynamical systems such as large neural networks. Here we point out that an easily computable subset of the critical manifold, the set of target points, can be used as a reference for the investigation of high–dimensional slow–fast systems. The set of target points corresponds in this context to the adiabatic projection of a given orbit to the critical manifold. Applying our framework to a simple recurrent neural network, we find that the scaling relation of the Euclidean distance between the trajectory and its target points with the control parameter of the slow time scale allows to distinguish an adiabatic regime from a state that is effectively independent from target points.

Keywords: transient state, slow–fast systems, recurrent neural network, chaos, target points

## I. INTRODUCTION

Coexisting fixed point attractors such as place cells [1] are commonly assumed to strongly influence cognitive processing in the brain, either alone [2] or in conjunction with feed–forward processing, with the latter being the case for the episodic memory [3]. A system characterized by a single fixed point attractor could however not be functional on its own, as it would depend on additional mechanisms to reset the dynamics. It is hence interesting, that neural activity characterized by transitions between multiple meta–stable attractors [4] has been discovered in the olfactory system of zebrafish [5] and in the gustatory cortex [6]. Similar transient state dynamics [7] is also found in resting state networks in low–frequency contributions of human fMRI data [8], where it enables processes that are associated with cognitive tasks even in the complete absence of external stimuli [9]. Resting–state brain networks also show complex spatio–temporal dynamics, in terms of transitions between states characterized by high and low functional connectivities, which resemble transiently existing attractor structures [10]. Such state–dependent fluctuations may play an important role in task–related brain computations [11] such as the interaction of motion and sensation (cf. [12]).

Dynamics involving switching transitions between transiently stable states has been addressed in the contexts of semantic learning in autonomously active networks [13, 14], within reservoir computing [15] and in networks dominated by heteroclinic orbits [16]. In case

of the latter, periodic orbits are formed when the dynamics follows heteroclinic connections between saddle points encoding information in the different states, which however exist only for symmetry–invariant networks. The details of the internal dynamics are on the other hand more difficult to analyze for the case of reservoir computing [17], for which large random network layouts are generically used.

It is well known that transiently attracting states are present in slow–fast systems [18–20], i.e. in dynamical systems with distinct time scales. The fixed points of the fast subsystem, which are formally destroyed by the slower subsystem, form in this case a manifold that appears under several distinct names in the literature, such as slow manifold [18] and critical manifold [19]. This manifold corresponds to transiently stable states, and it has a pronounced influence on the overall dynamics, which takes place mostly in the close vicinity to this manifold.

The switching dynamics of low dimensional slow–fast dynamical systems can be addressed analytically by singular perturbation theory [19, 21], which has been used to investigate a number of relaxation oscillators [22], such as the van–der–Pol oscillator and the FitzHugh–Nagumo model for the dynamics of a single neuron [20, 23, 24]. Further applications of singular perturbation theory include the study of small Hopfield–type neural networks [25], the analysis of the motion on the critical manifold [26], of the detailed influence of different time scales [27], and of the scaling behavior close to bifurcations [28, 29].

It is generally accepted that a complete hierarchy of time scales [30] is necessary to describe the different tasks and activity levels in the brain. Examples are working memory, short–term and long–term memory and a range

---

\* gros@th.physik.uni-frankfurt.de

of distinct types of neural plasticity [31]. Functional hierarchy in recurrent neural networks for motion tasks [32] is another phenomenon emerging from a separation of time scales.

### A. Adiabatic fixed points

We will start this study by considering attractor ruins [33] in slow–fast systems, i. e. systems that compose of a fast subsystem and an additional slow subsystem, both being coupled. Attractor ruins are the remnants of points that are fixed points in the fast subsystem, but stop being fixed points (i. e., they get “destroyed” or “ruined”) by the interaction with the additional slow process (or by noise in noisy setups).

Such states can be found in literature under various names, such as attractor relics [33, 34], transiently attracting states [34] and ghosts [35]. Attractor ruins are to be found on the critical manifold and are hence transiently attracting, but not asymptotically stable. They will strongly influence the dynamics of a system whenever the coupling to the perturbation is weak.

Attractor ruins are defined on the level of the full system, being however embedded in the phase space of the fast (decoupled) variables. Hence, as it has been recognized previously [33, 34], the evolution of attractor ruins can be cast in terms of a metadynamics of attractors, which is in turn important for the modeling of cognitive processes like memory or decision making.

The aim of this study is to investigate the effect of attractor ruins on the dynamics in the overall system. Therefore we present an efficient measure to determine the influence of the attractor ruins and distinguish different dynamical regimes by that.

Furthermore, we introduce here the generic term *adiabatic fixed point (AFP)*, denoting all fixed points of the fast system when the slow variables are fixed but otherwise arbitrary. All AFP form, by definition, the critical manifold. We note, however, that there are stable and unstable AFP.

### B. A reference manifold on the critical manifold

Most of the stable adiabatic fixed points have in general nothing to do with the long–term behavior of the system. We will define in this context the unique set of *target points* as a subset of AFP corresponding to a given trajectory. We shall concentrate on trajectories that evolve on an attractor of the full system, i. e., on periodic or chaotic orbits of the full system that are reached after prolonged times. For an arbitrary locus on such a trajectory, a target point will be defined as the corresponding point that would be approached under the time evolution with fixed slow variables.

As the shape of the manifold of target points only depends on the fast subsystem and the trajectory it cor-

responds to, this manifold can be used as a reference manifold for the motion of the full system. Since slow variables in real world applications are not infinitesimally slow, the distance between the trajectory and the respective target points, being larger than zero, is an important measure for the assessment of the influence a target point and hence the critical manifold as a whole exerts on the dynamics. The critical manifold is both uniquely defined and numerically accessible; the manifold of target points, being a subset of the critical manifold, is also uniquely defined, as it corresponds to a certain trajectory. Therefore we will use the manifold of target points in this approach as a low dimensional reference manifold to characterize the corresponding dynamics in a potentially high dimensional phase space.

### C. Adiabatic and non–adiabatic regimes

Analyzing the distance between a given orbit and its associated target points we discriminate two qualitatively different dynamical regimes:

- In the *adiabatic regime* the dynamics is effectively influenced by target points, with the average distance of the trajectory to the target points scaling with the ratio of the slow and the fast time scale. We emphasize that the dynamics of the slow subsystem does not vanish in the adiabatic regime. The term relates rather to a regime of parameters, for which the trajectory follows the target points (which are *adiabatic* fixed points) closely, interseeded with jumps between different branches of the critical manifold. The corresponding different branches of the manifold of target points represent different transiently attracting states.
- In the *non–adiabatic regime* the dynamics effectively decouples from the target points, with the distance to the target points being in essence invariant with respect to changes of the relative time scale.

One may discriminate equivalently between regimes in which a perturbation expansion in the slow time scale converges or diverges, respectively [19]. Our approach aims on the other hand to develop tools suitable for the numerical study of high–dimensional slow–fast systems. We find that the study of target points, which are straightforward to determine numerically, allows in this context to distinguish between the adiabatic and the non–adiabatic regime.

### D. Three–site recurrent neural networks

In the second part of this study we apply our framework to a network of continuous–time rate–encoding neurons, which has been shown previously to exhibit non–trivial dynamical states [36]. As we are mainly interested

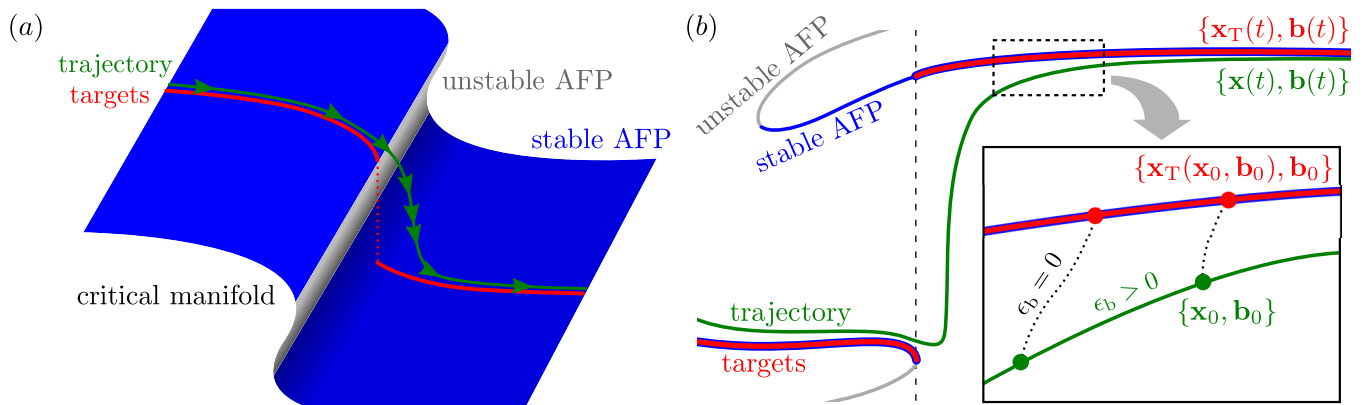


FIG. 1. Sketch of the effect of target points on a trajectory. (a) The target manifold (red line) is a subset of the manifold of all stable fixed points in the fast subsystem (blue sheets). Note that the critical manifold consists of stable AFP (blue surfaces) and unstable AFP (grey surface). The target points correspond uniquely to a given trajectory (green line), which follows the target points slightly delayed. (b) At every point  $\{\mathbf{x}_0, \mathbf{b}_0\}$  on the trajectory (green bullets in the inset) the fast subsystem  $\mathbf{x}(t)$  is attracted by the uniquely corresponding target point  $\{\mathbf{x}_T(\mathbf{x}_0, \mathbf{b}_0), \mathbf{b}_0\}$  (red bullets). For  $\epsilon_b = 0$  the system would converge (dashed lines) to the target point. For a finite flow in the slow subsystem  $\mathbf{b}(t)$ , viz when  $\epsilon_b > 0$ , the system evolves, on the other side, along the trajectory (green line). The set of target points corresponds to a map of the trajectory  $\{\mathbf{x}(t), \mathbf{b}(t)\}$  to the critical manifold.

in how AFP influence the intrinsic behavior of the network, we restrict ourselves to autonomously active networks, i.e. networks without external input. A separation between the time scale of the membrane potential and an intrinsic neural parameter, the threshold, is present in this system.

For concreteness we study a three–neuron network allowing for an in–depth understanding of the resulting dynamical states. Computing the transiently attracting states (as connected sets of target points) and the distance measures quantifying the influence of target points on the actual dynamics, leads to the characterization of two distinct dynamical regimes, i.e. the adiabatic and the non–adiabatic regime. We conclude with an analysis of the transition between these two regimes and of the role of target points for chaotic motion.

## II. THEORY — ATTRACTOR METADYNAMICS IN SLOW–FAST DYNAMICAL SYSTEMS

We consider with

$$\begin{aligned} \dot{x}_i &= f_i(\mathbf{x}, \mathbf{b}) \\ \dot{b}_j &= \epsilon_b g_j(\mathbf{x}, \mathbf{b}) \end{aligned} \quad (1)$$

$N + M$  dimensional slow–fast dynamical systems, where we have denoted with  $\mathbf{x} = \mathbf{x}(t) = \{x_i(t)\}_{1 \leq i \leq N}$  the fast variables and with  $\mathbf{b} = \mathbf{b}(t) = \{b_j(t)\}_{1 \leq j \leq M}$  the slow variables. The slow time scale is set by  $\epsilon_b$ , which is also the ratio of time scales.

The set of fixed points in the fast subsystem, i.e.  $d\mathbf{x}/dt = 0$  for given and fixed  $\mathbf{b}$ , is of special interest for the analysis of slow–fast dynamical systems. The entirety of these points, which are the intersections of the

nullclines  $dx_i/dt = 0$  of the fast subsystem [37], are generally termed slow manifold [18] or critical manifold [19]. Please note that the term slow manifold is used in different contexts and fields and also with different definitions as already pointed out by Lorenz [38] (cf. [18, 19, 21]). In the context of this work we will refer to the set of fixed points in the fast subsystem as critical manifold, as this nomenclature is widely used in the field. Here we constrain ourselves to a fast subsystem with only fixed point attractors. This is for instance the case if the fast subsystem is a gradient system, e.g. when the fast dynamics is derived from a generating functional [36, 39]. The different branches of the critical manifold are therefore exclusively composed of isolated fixed points. They are often well characterized, for real–world systems, in terms of their physical and/or neurobiological properties [8].

### A. Adiabatic fixed points (AFP) and target points

In physics terminology the limit  $\epsilon_b \rightarrow 0$ , i.e. when the slow subsystem is infinitely slow, is termed the adiabatic limit, such as in the Born–Oppenheimer approximation [40], where the slow movement of the atomic nuclei can be treated as parametric variables when addressing the relatively fast dynamics of the electrons. In the case  $\epsilon_b = 0$  the configuration  $\mathbf{b}$  of the slow subsystem is constant and can be treated as parameters. We will hence use the term adiabatic fixed point (AFP) for the fixed points of the fast subsystem. Note that the set of all AFP is equivalent to the critical manifold [19] of the system.

Considering a generic state  $\{\mathbf{x}_0, \mathbf{b}_0\}$  as the starting point of a solution  $\mathbf{x}(t')|_{\mathbf{b}=\mathbf{b}_0}$  of Eq. (1) for fixed slow

variables  $\mathbf{b} = \mathbf{b}_0$ , we define with

$$\mathbf{x}_T(\mathbf{x}_0, \mathbf{b}_0) = \lim_{t' \rightarrow \infty} \mathbf{x}(t')|_{\mathbf{b}=\mathbf{b}_0} \quad (2)$$

the fast component of the target point  $\{\mathbf{x}_T(\mathbf{x}_0, \mathbf{b}_0), \mathbf{b}_0\}$  corresponding to the respective starting point. Here we take  $\mathbf{x}_0 = \mathbf{x}(t_0)$  and  $\mathbf{b}_0 = \mathbf{b}(t_0)$  to be the fast and respectively slow components of a point on a trajectory  $\{\mathbf{x}(t), \mathbf{b}(t)\}$  in the full system, as parameterized by the time  $t = t_0$ . The mapping (2) is unique for a given pair  $(\mathbf{x}_0, \mathbf{b}_0)$ , depending furthermore not on  $\epsilon_b$ , which is the ratio of the time scales. All target points are AFP and a set of target points corresponding to a given trajectory is a subset of the critical manifold. This set of target points can thus be used as a reference manifold that allows to analyze the dynamics of the overall system relative to the critical manifold.

The relation of target points, trajectory and critical manifold is sketched schematically in Fig. 1 (b). We also present in Table I (cf. Appendix A) a pseudo-code for the numerical computation of AFP and target points.

## B. Kinetic energy of phase space evolution

Target points can be computed via a straightforward evolution of the equations of motion of the fast subsystem for fixed slow variables  $\mathbf{b}$ . Unstable adiabatic fixed points may be found [35], in addition, by minimizing the kinetic energy

$$q_x = \frac{\dot{\mathbf{x}}^2}{2} = \frac{1}{2} \sum_{i=1}^N \dot{x}_i^2 \quad (3)$$

of the flow in the fast subsystem. A minimum with  $q_x = 0$  corresponds to a fixed point of the fast subsystem, regardless of its stability. This is used to compute AFP numerically (cf. Appendix A).

The zeros of  $q_x$  are generically not minima of the kinetic energy  $q = (\dot{\mathbf{x}}^2 + \mathbf{b}^2)/2$  of the full system, for which also the flow in the slow subsystem,  $\dot{\mathbf{b}}$ , needs to vanish. The same holds for slow points, which are defined by a vanishing  $q_x$  and small values of  $q$ , see [35].

## C. Attractor metadynamics

The set of target points  $\{\mathbf{x}_T(t), \mathbf{b}(t)\}$ , where

$$\mathbf{x}_T(t) \equiv \mathbf{x}_T(\mathbf{x}(t), \mathbf{b}(t)) \quad (4)$$

corresponds to the mapping (2) of a trajectory  $\{\mathbf{x}(t), \mathbf{b}(t)\}$  onto the critical manifold. As mentioned before, we shall only consider trajectories on attractors for this study. The set of target points hence has the same dimensionality as the respective attractor, e.g. one dimensional for a limit cycle or fractal for a chaotic attractor (cf. Sect. III A). In typical slow-fast systems the

embedding dimension of the critical manifold is usually much lower than the dimension of the full system. The dimension of a set of target points corresponding to a given trajectory, being a subset of the critical manifold, is thus even lower, reducing therefore the complexity of the analysis.

One defines as attractor metadynamics the time evolution of the target points Eq. (4), which can be continuous or characterized by jumps between distinct sets of target points. Distinct branches of the critical manifold can often be classified in real world applications, e.g. in the neurosciences when using a slow feature analysis [41]. States on the same branch of the critical manifold are then lumped together, with distinct branches corresponding to different objects, such as ‘chair’ and ‘table’. Target points continuously connected, compare Fig. 1, can then be considered a set of states corresponding to the same object and hence as a transiently attracting state. The mapping (4) therefore implies that the flow moves from one transiently attracting state to another whenever the respective target point jumps from one branch of the critical manifold to the next. This classification is considered important especially in the neurosciences, where attracting states guide decision making, memory storage and recognition [4].

## D. Distance to target points

As a measure of the influence a given target point exerts on the trajectory we will consider the Euclidean distance  $d(t)$ ,

$$d(t) = \sqrt{(\mathbf{x}(t) - \mathbf{x}_T(t))^2}, \quad \langle d \rangle = \frac{1}{\tau} \int_0^\tau dt d(t) \quad (5)$$

between the fast components of the trajectory  $\{\mathbf{x}(t), \mathbf{b}(t)\}$  and the corresponding target points  $\{\mathbf{x}_T(t), \mathbf{b}(t)\}$ , see Eq. (4). The corresponding time-average  $\langle d \rangle$  has been defined in (5) for the case of a limit cycle with period  $\tau$ , with a corresponding straightforward generalization for chaotic attractors.

The average distance  $\langle d \rangle$  vanishes, per construction, in the adiabatic limit  $\epsilon_b \rightarrow 0$ . For finite  $\epsilon_b > 0$  we find, on the other hand, two regimes, with  $\langle d \rangle$  scaling with  $\epsilon_b$  in the *adiabatic regime*, but not in the *non-adiabatic regime*.

Apart from the average distance  $\langle d \rangle \rightarrow 0$ , one can also evaluate the probability density function  $\rho(d)$  of the distances over a given attractor. The corresponding cumulative distribution function of distances

$$P(d) = \int_0^d du \rho(u) \quad (6)$$

can then be used to characterize regimes. As a trajectory stays close to the target points for prolonged time spans

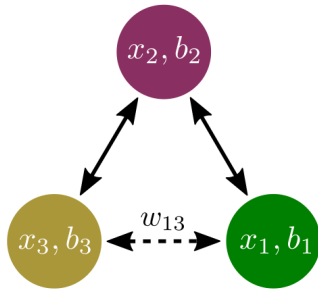


FIG. 2. Scheme of the three–neuron system. The second neuron (top) is exciting the other two neurons (solid arrows) and vice versa. The first and the third neuron (bottom) are coupled by an inhibitory connection  $w_{13} < 0$  (dashed arrow).

in the adiabatic regime one finds contributions at small distances  $d \sim \epsilon_b \ll 1$  for the cumulative distribution. A second contribution comes from the jumps between the different branches of target points at larger distances  $d \gg \epsilon_b$  (usually  $d \sim 1$ ). However, in the non–adiabatic case only the latter contribution, at larger distances, exists, as the system comes close to the target points only occasionally. A lack of contributions at small distances  $d \sim \epsilon_b$  is an evidence that the dynamics is in the non–adiabatic regime.

### III. RESULTS

#### A. Three–neuron system

To investigate the effect of target points on the overall dynamics, we consider for this study a small neural network (cf. Fig. 2) of three rate–encoding continuous–time point neurons [36]. Networks of three neurons have already served as model systems in different contexts such as modeling pacemaker circuits [42], the stomatogastric ganglion in lobster [43] or neural motifs [44]. Here we chose the three–neuron layout to study the fundamental properties of AFP and target points, as it allows for a full investigation of its non–trivial dynamics and phase diagram.

The fast subsystem corresponds in this case to the time evolution

$$\dot{x}_i = -x_i + \sum_{j=1}^N w_{ij} y_j, \quad (7)$$

of the membrane potential  $x_i$ , with  $w_{ij} > 0$  and  $w_{ij} < 0$  denoting excitatory and inhibitory connection  $j \rightarrow i$  respectively. The corresponding firing rate  $y_i \in [0, 1]$ , the neural activity, is a sigmoidal function of the respective membrane potential:

$$y_i = \frac{1}{1 + \exp(a_i(b_i - x_i))}. \quad (8)$$

We have used constant gains  $a_i \equiv a = 6$ , whereas the threshold  $b_i = b_i(t)$  is adapting slowly [45] on extended time scales  $1/\epsilon_b \gg 1$ ,

$$\dot{b}_i = \epsilon_b 2a(y_i - 1/2). \quad (9)$$

In the context of this model the ratio of times scales  $\epsilon_b$  is also called the adaption rate of the slow variables  $b_j$ . The time evolution Eq. (9) of the slow variables attempts to drive the dynamics towards  $y_i \rightarrow 1/2$  as  $\dot{b} \rightarrow 0$ , which is the fixed point of the full system (cf. Appendix B).

The state of a neuron is hence described by the tuple  $\{x_i(t), b_i(t)\}$ . For the particular three–neuron system sketched in Fig. 2, the dynamics of the fast variables  $x_i$  is given by [33]

$$\begin{aligned} \dot{x}_1 &= -x_1 + y_2 + w_{13}y_3 \\ \dot{x}_2 &= -x_2 + y_1 + y_3 \\ \dot{x}_3 &= -x_3 + y_2 + w_{13}y_1, \end{aligned} \quad (10)$$

with  $w_{13} = w_{31} < 0$  being inhibitory. All remaining synaptic weights are unity  $w_{12} = w_{21} = w_{23} = w_{32} = 1$  and thus excitatory connections. For the results presented here we computed the numerical solution of the ODE system Eqs. (9) and (10) performing a fourth order Runge–Kutta integration algorithm with Fehlberg tableau [46] using step size  $dt = 10^{-2}$ . For computing the AFP we used a minimization algorithm with a BFGS strategy [47, 48] provided by the `dlib` optimization library [49] for the C++ programming language.

#### 1. Symmetries

The network shown in Fig. 2 is symmetric under the exchange  $1 \leftrightarrow 3$  of the first and the third neuron, a reflection symmetry. For the special case  $w_{13} = -1$  the additional  $C3$  rotational symmetry  $\mathbf{x} \rightarrow \tilde{\mathbf{x}}$  and  $\mathbf{b} \rightarrow \tilde{\mathbf{b}}$ , with

$$\begin{aligned} \tilde{x}_1 &= -x_3, & \tilde{x}_2 &= x_1 + 1, & \tilde{x}_3 &= x_2 - 1 \\ \tilde{b}_1 &= -b_3, & \tilde{b}_2 &= b_1 + 1, & \tilde{b}_3 &= b_2 - 1 \end{aligned} \quad (11)$$

is present. Eq. (11) can be verified by inspecting Eqs. (9) and (10). This leads to

$$\tilde{y}_1 = 1 - y_3, \quad \tilde{y}_2 = y_1, \quad \tilde{y}_3 = y_2. \quad (12)$$

Applying this iteration three times yields the identity transformation, Eq. (11) is hence equivalent to a  $C3$  symmetry.

#### 2. Dynamics of the three–neuron system

Before analyzing the transiently attracting states of the three–neuron system we briefly discuss here the possible types of long–term dynamics in the network, i. e. attractors in the phase space of the full system, for different cases of the inhibitory weight  $w_{13}$  and of the time scale difference  $\epsilon_b$ .

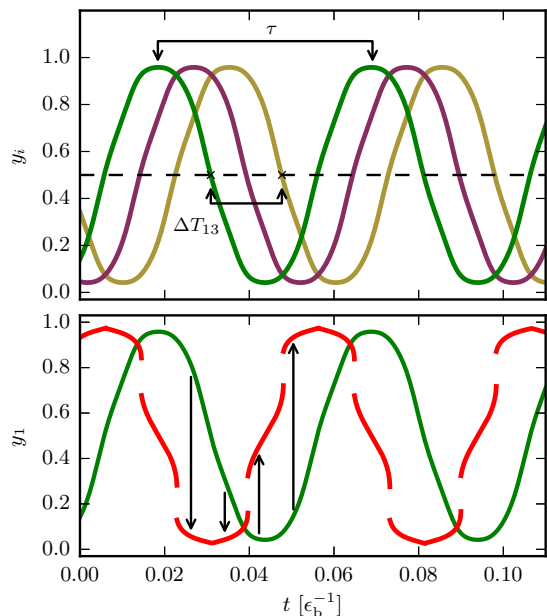


FIG. 3. Firing rates of the three neurons for  $\epsilon_b = 8 \cdot 10^{-4}$  in the  $C3$  symmetric case  $w_{13} = -1$  (indicated by the magenta bullet in Fig. 5) over rescaled time. (*top*) Green/violet/yellow denote  $y_1/y_2/y_3$ ; the relative phase shift  $\Delta_{13} = \Delta T_{13}/\tau = 1/3$  is the ratio of the time shift  $\Delta T_{13}$  between two consecutive Poincaré sections  $y_i = 1/2$ ,  $\dot{y}_i < 0$  of the first and third neuron, and the oscillation period  $\tau$ . (*bottom*)  $y_1$ -component of the target points (red) and of the trajectory (green), with the arrows indicating the behavior of the system in the adiabatic limit  $\epsilon_b \rightarrow 0$  (cf. Fig. 1).

*a. C3 symmetry* Due to the  $C3$  symmetry of the three-neuron system for  $w_{13} = -1$  discussed in Sect. III A 1, we find a traveling wave solution where all neurons show the same activities  $x_i(t) = x(t - \theta_i)$  with period  $\tau$ , albeit with distinct phases  $\theta_i$ , shifted respectively by  $\tau/6$ . One can easily prove that this type of motion is always an exact solution in the case of  $w_{13} = -1$  (cf. Appendix C).

In the top panel of Fig. 3 we show an example of the traveling waves solution for  $w_{13} = -1$ ,  $\epsilon_b = 8 \cdot 10^{-4}$  with green/violet/yellow encoding  $y_1/y_2/y_3$ . Time has been rescaled with respect to  $1/\epsilon_b$ . For a further quantification we define the dimensionless relative phase shift

$$\Delta_{13} = \Delta T_{13}/\tau \quad (13)$$

between the first and the third neuron, where  $\Delta T_{13}$  is the time difference of two consecutive intersections of  $y_1$  and  $y_3$  with the Poincaré plain  $y_i = 1/2$ ,  $\dot{y}_i < 0$  (cf. top panel of Fig. 3). The traveling waves solution is characterized hence by  $\Delta_{13} = 1/3$ .

The traveling waves motion is an exact solution for all  $\epsilon_b$ , but stable only for  $\epsilon_b > 6 \cdot 10^{-5}$ . For all  $\epsilon_b > 6 \cdot 10^{-5}$  the motion is hence symmetry protected [50] in the sense that the relative phase shift (13) is independent of  $\epsilon_b$ , viz  $\Delta_{13} \equiv 1/3$ .

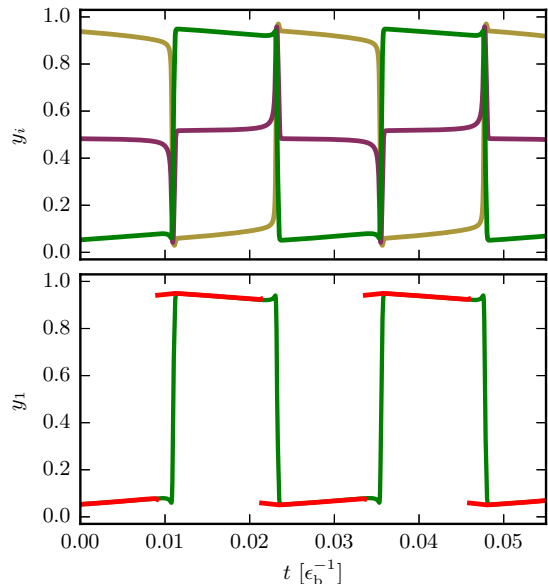


FIG. 4. Firing rates of the three neurons for  $\epsilon_b = 10^{-5}$  in the  $C3$  symmetric case  $w_{13} = -1$  (indicated by the cyan square in Fig. 5) over rescaled time. (*top*) green/violet/yellow denote  $y_1/y_2/y_3$ . (*bottom*) the  $y_1$ -component of the target points (red) and of the trajectory  $y_1$  (green). The system performs an anti-phase flip-flop oscillation of the first and the third neuron,  $\Delta_{13} = 1/2$ .

In the top panel of Fig. 4 we show the trajectory for  $\epsilon_b = 10^{-5}$ , viz in the phase where the traveling wave solution is not anymore stable. The activity levels of the first and the third neuron now approach mutually either full or low activity states,  $y_i \approx 1$  and  $y_i \approx 0$  respectively, while the second neuron stays mostly at  $y_2 \approx 1/2$  (half active). The relative phase shift is  $\Delta_{13} = 1/2$ , which is the maximal possible value.

The system thus flips between the two states  $\mathbf{y} = (y_1, y_2, y_3) \approx (0, 1/2, 1)$  and  $\mathbf{y} \approx (1, 1/2, 0)$ . The flipping time of this flip-flop oscillation scales inversely with the adaption rate  $\epsilon_b$ .

*b. No C3 symmetry* In Fig. 5 we outline the distinct dynamical regimes observed for the general case of arbitrary inhibitory weights close to the symmetric case. The relative phase shift  $\Delta_{13}$  is color-coded and shown as a function of the adaption rate  $\epsilon_b$  and of the inhibitory weight  $w_{13}$ .

On the horizontal center axis  $w_{13} = -1$ , which represents the case of a  $C3$  symmetric system, the symmetry protected traveling wave solution with  $\Delta_{13} = 1/3$  occurs for  $\epsilon_b > 6 \cdot 10^{-5}$  (cf. Fig. 3) and the flip-flop oscillation  $\Delta_{13} = 1/2$  for  $\epsilon_b < 6 \cdot 10^{-5}$  (cf. Fig. 4).

Far off the symmetric axis only two possible states exist: either the system performs a flip-flop oscillation ( $\Delta_{13} = 1/2$  and  $w_{13} < -1.15$ ) or an in-phase oscillation ( $\Delta_{13} = 0$  and  $w_{13} > -0.85$ ). In the latter case all three neurons fire synchronously and switch between a state

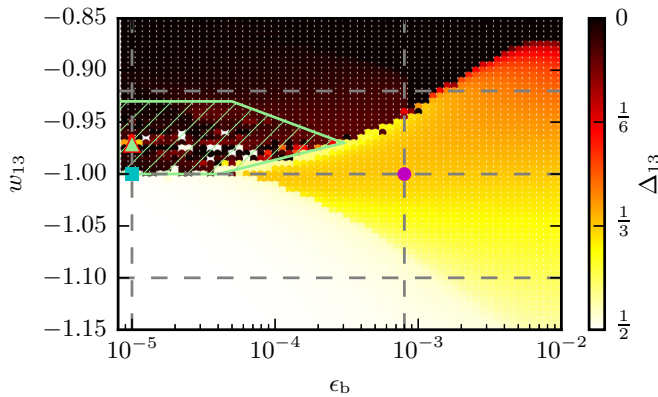


FIG. 5. Phase diagram, as a function of the adaption rate  $\epsilon_b$  and of the inhibitory weight  $w_{13}$ , where the color encodes the phase difference  $\Delta_{13}$  of the first and the third firing rate of the neuron, normalized with the period of the oscillation (color bar; compare Eq. (13)). The two main regimes show in-phase oscillations  $\Delta_{13} = 0$  of all neurons (dark) or anti-phase oscillation  $\Delta_{13} = 1/2$  of neurons 1 and 3 (bright). Close to the symmetric axis  $w_{13} = -1$  there exists a region in the parameter space with phase shifts in between these extreme cases. The dashed gray horizontal lines mark the cuts through the parameter section considered in Figs. 7, 8 and 6 (left panel). The solutions corresponding to the magenta bullet ( $\epsilon_b = 8 \cdot 10^{-4}$ ,  $w_{13} = -1$ ) and to the cyan square ( $\epsilon_b = 10^{-5}$ ,  $w_{13} = -1$ ) are shown in Fig. 3 and Fig. 4 respectively. Disperse patches of chaotic motion can be found in the green shaded area. One example is the red framed triangle ( $\epsilon_b = 10^{-5}$ ,  $w_{13} = -0.9709$ ; compare Fig. 10).

$\mathbf{y} \approx (1, 1, 1)$  of high activity and a state  $\mathbf{y} \approx (0, 0, 0)$  of low activity.

These two main types of motion follow directly from the topology of the network illustrated in Fig. 2. For relatively strong inhibition  $w_{13} < -1$  the first and the third neuron suppress each other mutually, they can therefore not be active at the same time. A dominance of inhibition thus leads to a flip-flop oscillation. Weak inhibition  $w_{13} > -1$  allows on the other side both the first and the third neuron to be active at the same time, and therefore also the second neuron, leading to an in-phase oscillation of all three neurons.

The situation is more complicated in the inner region of  $-1.15 < w_{13} < -0.85$  (cf. Fig. 5), where inhibitory and excitatory weights are similar in magnitude. The relative phase shift  $\Delta_{13}$  varies continuously from its maximal value  $1/2$  to its minimal value  $0$ , when increasing  $w_{13}$  for  $\epsilon_b > 6 \cdot 10^{-5}$ , taking the value  $\Delta_{13} = 1/3$  right at the symmetry point  $w_{13} = -1$ , where the traveling wave solution, illustrated in Fig. 3 exists.

Below, we will discuss further horizontal and vertical cuts through parameter space, indicated by the dashed gray lines in Fig. 5, as well as the occurrence of chaotic attractors for certain parameter values to be found in the area that is green shaded in Fig. 5.

In Fig. 6 we present the sketch of the behavior along the previously mentioned two cuts of the phase diagram

for  $\epsilon_b = 10^{-5}$  and  $\epsilon_b = 8 \cdot 10^{-4}$  (cf. Fig. 5). For low adaption  $\epsilon_b = 10^{-5}$  as shown in Fig. 6 (a) we only find adiabatic behavior: either anti-phase oscillations (*i, iii*) or in-phase oscillations (*v*). Close to the symmetric transition point  $w_{13} = -1$  both types of attractors can be found depending on the initial conditions. As mentioned before, the anti-phase oscillation corresponds to a switching between the two anti-symmetric transiently attracting states  $\mathbf{y} \approx \{0, 1/2, 1\}$  and  $\mathbf{y} \approx \{1, 1/2, 0\}$ . In the case of the in-phase oscillation this is a periodic switching between the symmetric transiently attracting states  $\mathbf{y} \approx \{0, 0, 0\}$  and  $\mathbf{y} \approx \{1, 1, 1\}$ . For low adaption rate we thus find a direct transition between the two different types of attractors of the adiabatic regime. With a larger adaption  $\epsilon_b = 8 \cdot 10^{-4}$  in Fig. 6 (b) at the transition from strong inhibition to weak inhibition the traveling waves regime appears. The panels in Fig. 6 (b) depict five examples in the transition from anti-phase (*i*), via traveling waves (*ii-iv*), to in-phase oscillation (*v*). In the extreme cases of  $w_{13} = -1.1$  and  $w_{13} = -0.92$  we can guess once again that the firing rate is shaped by the anti-symmetric and the symmetric transiently attracting states respectively. In contrast to the case of lower adaption here we find that the transition between the in-phase and the anti-phase oscillation of the adiabatic regime happens via the non-adiabatic regime when passing the region of symmetry protection close to the symmetric case  $w_{13} = -1$ .

## B. Transiently attracting states in the three-neuron system

In the bottom panels of Figs. 3 and 4 we present the firing rate  $y_1$  of the first neuron (green) and the  $y_1$  component of the corresponding target point (red bullets and line), with the adiabatic evolution indicated by the black arrows.

- For  $\epsilon_b = 8 \cdot 10^{-4}$ , the non-adiabatic case shown in Fig. 3, we find that the set of target points splits into four branches. The jumps between the distinct branches are however not directly visible in the original trajectory, which is almost completely decoupled of the dynamics of the target points.
- For  $\epsilon_b = 10^{-5}$ , a case from the adiabatic regime illustrated in Fig. 4, we observe on the other hand only two branches of target point manifolds. For extended time spans the trajectory follows closely the critical manifold, jumping however periodically between the two distinct branches.

One observes in Fig. 4, that the orbit needs a certain time, a delay, to leave a given branch of the target point manifold. This is a phenomenon typical for systems with multiple time scales [28].

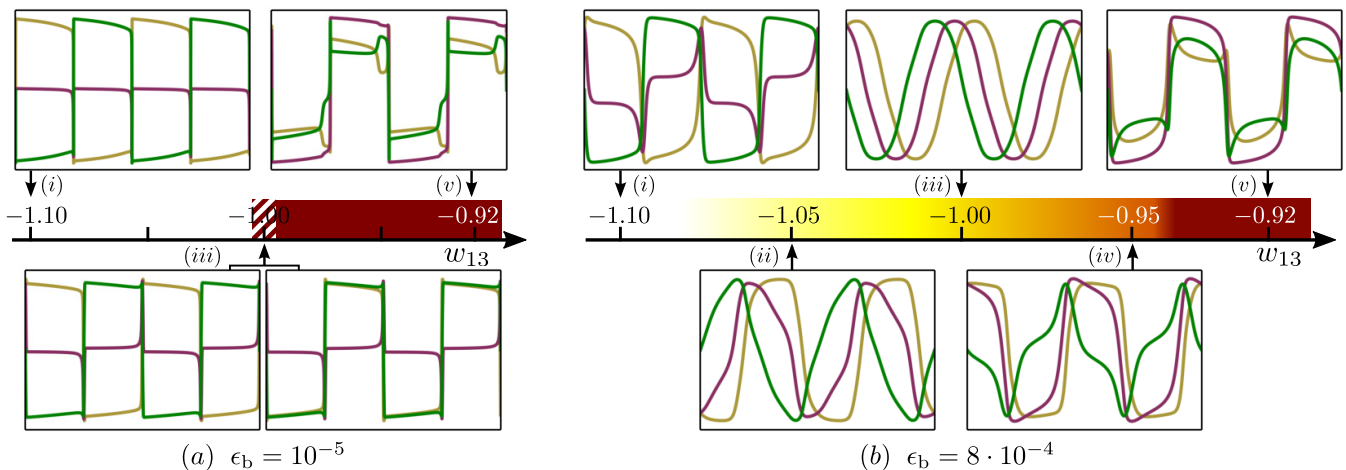


FIG. 6. Vertical cuts through the phase diagram shown in Fig. 5. The color of the bar encodes the phase shift  $\Delta_{13}$  as a function of  $w_{13}$ . The insets show the firing rates of all three neurons (cf. the upper panels of Figs. 3 and 4). (a) For  $\epsilon_b = 10^{-5}$  the transition from anti-phase to in-phase oscillations occurs near the symmetric point  $w_{13} = -1$ . The area marked by stripes shows bistability and both types of attractors coexist. (b) For  $\epsilon_b = 8 \times 10^{-4}$  the firing rates change in a smooth manner from anti-phase oscillation to traveling waves, and with a small jump to in-phase behavior.

### 1. Stable and unstable adiabatic fixed points

In Fig. 7, which illustrates the dynamics along the horizontal cut through the phase diagram for  $w_{13} = -1$ , the adiabatic fixed points for five different values of the adaption rate are shown. Here we have included all adiabatic fixed points, including the unstable ones, which we have found by minimizing Eq. (3). Each of the five insets shows a sketch of the trajectory (green), target points (red), other stable AFP (blue) and saddle AFP (gray) in the activity  $y_1$  of the first neuron (cf. bottom panels of Figs. 3, 4). Each of these insets serves as an example of the five different phases that can be distinguished by the shape and stability of the AFP. The whole non-adiabatic regime with phase shift  $\Delta_{13} = 1/3$  is marked by the yellow bar, while the adiabatic regime with  $\Delta_{13} = 1/2$  is indicated by a brown bar. The range of occurrence in the adaption rate  $\epsilon_b$  of the four non-adiabatic phases is indicated by the gray bars included in the yellow bar.

Starting at relatively high adaption  $\epsilon_b = 10^{-2}$  in Fig. 7 panel (v) we find only stable AFP of which all act as target points and the attractor metadynamics therefore is continuous. Decreasing the adaption rate  $\epsilon_b$  (cf. panels (iv) to (i)) we observe the occurrence of saddle type AFP and stable AFP which are no targets to the trajectory.

In panels (i-iii) of Fig. 7 one can find saddle-node bifurcations, in which stable (blue) and saddle type (gray) AFP merge. The saddle-node bifurcation points originate from a cusp bifurcation [51] on the critical manifold, with the slow variables as bifurcation parameters. The adaption rate  $\epsilon_b$  determines at which point the trajectory crosses the cusp bifurcation. Thus one either finds a continuous manifold of target points or jumps.

This change in the structure of the corresponding target points with the adaption rate also affects the attrac-

tor metadynamics, which becomes discontinuous as well.

- For all adaption rates  $\epsilon_b > 6 \cdot 10^{-5}$  we find stable traveling waves solutions with a relative phase difference  $\Delta_{13} = 1/3$ , for which the trajectory is only marginally influenced by the transiently attracting states. This is the non-adiabatic regime (yellow bar).
- For lower adaption rates  $\epsilon_b < 6 \cdot 10^{-5}$  we find that both the trajectory and the attractor metadynamics perform flip-flop oscillation with a relative phase difference  $\Delta_{13} = 1/2$ . Here, in the adiabatic regime (brown bar), the motion follows strictly the metadynamics of the target points with some delay at the jumps, as mentioned earlier.

We emphasize that the transition between the adiabatic and non-adiabatic regime occurs at a remarkably low value of the adaption rate  $\epsilon_b \approx 6 \cdot 10^{-5}$ . The traveling wave solution being stable for  $\epsilon_b > 6 \cdot 10^{-5}$  is hence strongly protected by the C3 symmetry of the system. Off symmetry, i. e. for  $w_{13} \neq -1$ , the transition between the adiabatic and the non-adiabatic regime may become continuous (compare Fig. 5), and shifts to higher values in  $\epsilon_b$ . Along the symmetric axis  $w_{13} = -1$  we find a small region in the adaption rate  $\epsilon_b$  close to the transition, as marked by stripes in Fig. 7, where attractors from both the adiabatic and the non-adiabatic regime coexist. Starting close to an attractor from the non-adiabatic regime we can trace the non-adiabatic regime decreasing the adaption rate  $\epsilon_b$  in small steps. This procedure succeeds up to a certain value of  $\epsilon_b$ , depending on the precision of the computation and the step size in  $\epsilon_b$ , before ending up in an attractor of the adiabatic regime. Vice versa we can start from the adiabatic regime and trace

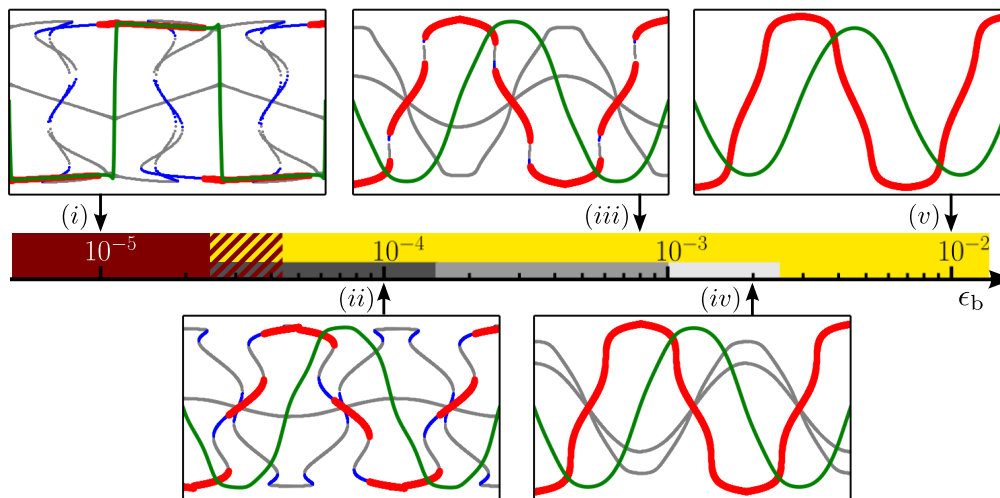


FIG. 7. Horizontal cut through the phase diagram shown in Fig. 5 at the  $w_{13} = -1$  value. The color of the bar encodes the phase shift  $\Delta_{13}$  as a function of adaption rate  $\epsilon_b$  (brown:  $\Delta_{13} = 1/2$ , yellow:  $\Delta_{13} = 1/3$ ). There are five phases to be distinguished by the stability and the shape of the AFP. Each phase is represented by a characteristic trajectory–AFP–plot in  $y_1$  (cf. Fig. 3 and 4 bottom row), the range of occurrence for the middle three is indicated by the gray bars within the yellow bar. Green/red/blue/gray in the plots denote the trajectory/target points/other stable AFP/unstable AFP respectively. For relatively large values of the adaption rate  $\epsilon_b$  (v) there are only stable AFP, acting as the target points. Decreasing  $\epsilon_b$  saddle AFP and non–target stable AFP occur (i–iv). Hysteresis in the transition is observed in the striped area.

it increasing  $\epsilon_b$ . This means we can observe hysteresis in the bistable transition region between the regimes.

## 2. Evolution of the average distance between trajectory and target points

Fig. 8 shows the average distance  $\langle d \rangle$ , as defined by Eq. (5), of the trajectory to the target points. Shown are horizontal cuts through the phase diagram Fig. 7, along  $w_{13} = -1.1$ ,  $-1$  and  $-0.92$ . In the absence of  $C3$  symmetry, the separation of time scales between fast and slow variables starts to fail for larger values of the adaption rate,  $\epsilon_b > 10^{-3}$ , with the distance  $\langle d \rangle \approx 1$  becoming independent of  $\epsilon_b$ .

An adiabatic regime is always observed for low adaption rates  $\epsilon_b$ . It is however clearly evident from Fig. 8 that the adiabatic regime is pushed down for the symmetric case  $w_{13} = -1$ , by more than one order of magnitude. States protected by symmetry operations, in our case the traveling wave solution illustrated in Fig. 3, can be exceedingly stable.

The discontinuous transition between the two regimes in the symmetric case  $w_{13} = -1$  is confirmed by both Fig. 5 and Fig. 8. There is a transition region in  $\epsilon_b$ , where two arbitrarily close initial conditions can show fundamentally different dynamics being in the adiabatic and the non–adiabatic regime, respectively (cf. Fig. 7 and the related discussion). On the two sides of this transition region, only one of these two different kinds of dynamics exists. Lacking any intermediate kind of dynamics, this abrupt transition is remarkable since the

shape of the AFP manifold does not depend on the adaption rate  $\epsilon_b$  at all. We thus stress that the distance to the reference manifold of target points, which is unique for given parameter values and initial conditions, reveals a qualitative change in the dynamics.

## 3. Statistics of the distance between trajectory and target points

For the same parameters as used in Figs. 3 and 4 we present in Fig. 9 the cumulative distribution function  $P(d)$  of the distance  $d$ , as defined by Eq. (6), between the trajectory and the corresponding target points. First the relative density  $\rho(d)$  of distances averaged over a given attractor is computed numerically by sampling the measured distances to 400 bins on the logarithmic range  $d \in [10^{-5}, 2]$ . To obtain the cumulative distribution of distances the density is then integrated as defined by Eq. (6).

For the non–adiabatic case (magenta) we find that there are only contributions in a narrow region  $d \in [0.7, 1.0]$  close to unity, resulting in turn from small residual variations of distance. For the adiabatic case (cyan) we observe substantial contributions both close to unity, reflecting the jumps between different target branches, and extended contributions from small distances  $d < 10^{-2}$ , which result from the evolution close to the AFP manifold. The difference between the adiabatic and the non–adiabatic regime shows up prominently in the statistics of the distances between trajectory and target points.

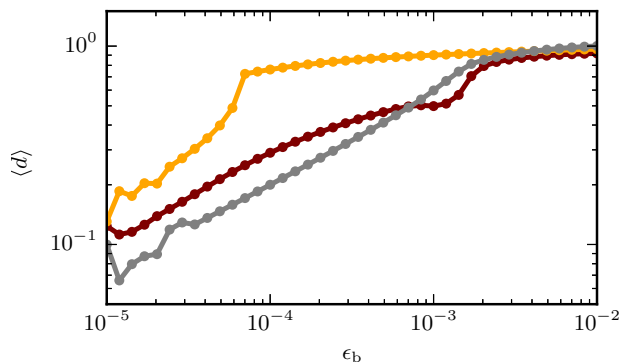


FIG. 8. Average distance  $\langle d \rangle$  of the trajectory to the corresponding targets, as defined by Eq. (5). Shown are horizontal cuts through the phase diagram, Fig. 5, along  $w_{13} = -1.1$  (gray),  $-1$  (yellow) and  $-0.92$  (brown). The regime is non-adiabatic, when the distance becomes independent of  $\epsilon_b$ , as it happens for larger values of the adaption rate. The system is adiabatic, conversely, when the distance scales with  $\epsilon_b$ , which happens for the symmetric case  $w_{13} = -1$  only for low adaption rates.

#### 4. Target points corresponding to chaotic motion

For a small region in the adiabatic regime  $\epsilon_b < 3 \cdot 10^{-4}$  and near the symmetric case,  $w_{13} \in [-1, -0.93]$ , we find patches in the parameter space that exhibit chaotic motion. An example is shown in Fig. 10 for  $\epsilon_b = 10^{-5}$  and  $w_{13} = -0.9709$ . The trajectory and the corresponding target points are shown both as a time series (left panel) and projected to the  $y_2 - y_1$  plane in phase space. Applying a recently developed 0–1 test for chaos, based on the cross–distance scaling of initially nearby trajectories [52], we find that this attractor is indeed chaotic.

Except for some overshooting, the trajectory shows a similar behavior to the adiabatic motion presented in Fig. 4, approaching the target point manifold and staying then close to it as long as it remains stable.

The manifold of target points has a highly non–trivial structure for the chaotic motion, in contrast to the piecewise smooth and periodic structure observed for the case of limit cycle attractors, as observed e.g. in Fig. 7. A visual inspection indicates (see the inset in the right–hand panel of Fig. 10) that the phase space projection of the target points forms a fractal structure. We did not attempt to directly compute the fractal dimension of the manifold of target points shown in Fig. 10, as this is computationally highly demanding. Chaotic behavior, on the other hand, is typically linked to the presence of fractals in the dynamical behavior [53].

Speaking in terms of transiently attracting states this means that in case of chaotic motion we cannot describe the motion as switching between two transiently attracting states. But rather we find that there must be infinitely many branches of transiently attracting states forming a fractal set. One may nevertheless cluster these fractal sets into two broad classes, corresponding to small

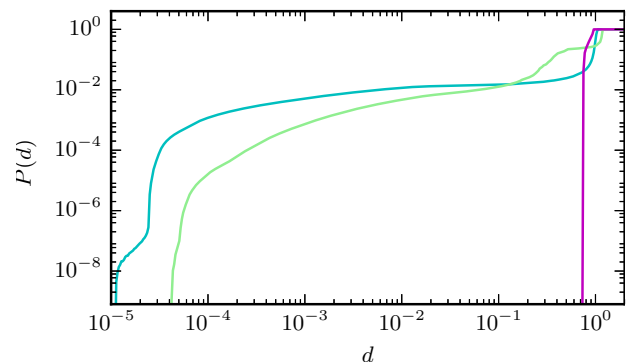


FIG. 9. The cumulative distribution function  $P(d)$  of the distance  $d$  between trajectory and the corresponding target point, as defined by Eq. (6), for the adiabatic case ( $\epsilon_b = 10^{-5}, w_{13} = -1$ , cyan), the non-adiabatic case ( $\epsilon_b = 8 \cdot 10^{-4}, w_{13} = -1$ , magenta), and for the chaotic attractor ( $\epsilon_b = 10^{-5}, w_{13} = -0.9709$ , light green; compare Fig. 10). For the non-adiabatic case there are only contributions close to unity ( $\langle d \rangle = 0.89$ ). Contributions from significantly smaller distances are observable in addition both for the adiabatic case ( $\langle d \rangle = 0.16$ ) and for the chaotic attractor ( $\langle d \rangle = 0.25$ ). The latter one has contributions also for intermediate distances  $d$ .

and large  $y_2$  respectively. A possible interpretation of that behavior includes a chaotic motion of the overall system driving the dynamics along the critical manifold, which itself does not have a fractal structure. Thus the irregular motion near the critical manifold results in a fractal set of target points. We emphasize that the target points themselves are always stable fixed points of the fast subsystem, for any values of the slow variables.

In order to compare the chaotic motion more precisely to the adiabatic and the non-adiabatic regimes, we have included in Fig. 9 the cumulative distribution function of distances (light green line) for the chaotic attractor. Besides the contribution close to unity due to the large distance jumps between different AFP branches, it reveals contributions at small distances  $d < 10^{-2}$ , which are significant also for the adiabatic case (cf. to cyan line). In this respect the chaotic attractor is close to the adiabatic regime. We find however additional medium size contributions  $d \approx 0.3$  that result from smaller jumps within the fractal set of target branches.

The chaotic dynamics thus goes through an infinite series of transient states, trying to stay close to the critical manifold (itself having a simple, not fractal geometry), which is also confirmed by the distribution of distances to the target points. We do not observe chaotic exploration of the phase space, i.e. long detours leading away from the target points as one could imagine for chaotic dynamics. Due to the relatively small adaption rate the chaotic dynamics is guided along different branches of the target manifold — similar to the regular adiabatic motion presented in Fig. 4.

Keeping on the other hand in mind that the inhibitory weight  $w_{13} = -0.9709$  is only slightly off the symmetric

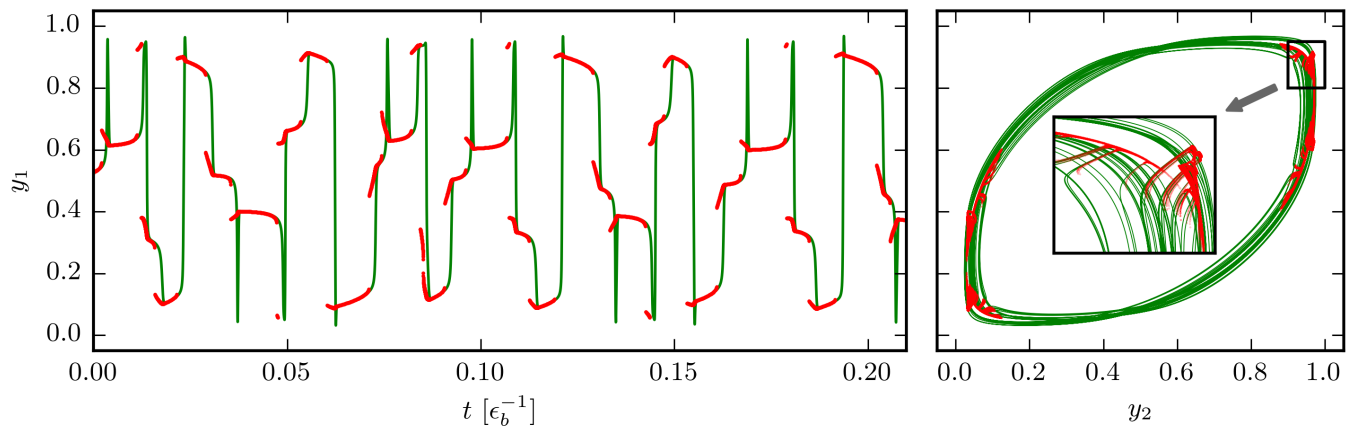


FIG. 10. Chaotic attractor (green) of the three-neuron system for  $\epsilon_b = 10^{-5}$ ,  $w_{13} = -0.9709$  (indicated by the red framed triangle in Fig. 5) with the corresponding target points (red). Shown are the firing rate  $y_1$  of the first neuron over time (*left*) and the projection of the orbit to the  $y_1 - y_2$  plane (*right*). The activity of the neuron is attracted towards fragments of the target point manifold, performing smaller and larger jumps between these fragments. The inset in the right-hand panel corresponds to a zoom-in to a region of target points, which on visual inspection seem to form a fractal structure.

case, it is to be expected that the shape of the critical manifold only changes smoothly in  $w_{13}$ . Therefore we would expect the same qualitative properties for the dynamics, i. e. the trajectory moving mostly close to branches of the target point manifold, as in the symmetric case presented in Fig. 4. But the origin of the chaotic dynamics is thus not obvious.

#### IV. DISCUSSION AND CONCLUSIONS

We have proposed here that the study of adiabatic fixed points and transiently attracting states, which are sets of target points, are useful when trying to understand complex slow-fast systems. As these can be realized by adding an additional slow component to an attractor network, the target points have a well defined physical function representing, e. g., as cognitive states in a neural network. Both the location in phase space and the topology of the manifold of target points can be easily evaluated without explicit knowledge of the full set of fixed points in the fast subsystem. The mapping of a given trajectory onto the corresponding set of target points is, by definition, unique and does not depend on the time evolution on the slow time scale. Thus target points qualify as a unique reference manifold for the overall dynamics. Transitions between smooth subsections of the manifold of target points correspond generically to transitions between well defined biological, physical or cognitive states.

We have shown, analyzing a three-site network of adapting rate-encoding neurons, that system symmetries may stabilize peculiar solutions which effectively decouple from the dynamics of target points. This decoupling shows up also in the statistics of the Euclidean distance between the trajectory and the respective target points. The distance distribution can be used furthermore to

classify states in terms of the relevance of the reference manifold.

We applied our analysis both to limit cycle and to chaotic dynamics. The detailed analysis of the latter phenomenon is a possible subject of future work. We find, somewhat surprisingly, that a fractal set of target points may guide chaotic behavior.

The above-described phenomenon is not to be confused with the case when the attractor of the fast subsystem is more complicated than a fixed point, e. g. limit cycles or chaotic attractors. In future studies the above described method for distinguishing dynamical regimes by means of target (fixed) points could be generalized to arbitrary target attractors. The key implication then will be to generalize the distance measurement between a trajectory and the corresponding attractor.

Our approach assumes a separation of time scales to be present, breaking down once the time scales for the slow and for the fast subsystem approach each other. The ability to treat the system analytically is however not needed.

We believe, in conclusion, that the study of target points could provide additional insights especially for slow-fast dynamical systems with a relatively high number of degrees of freedom. These points can serve as a unique reference to investigate the overall dynamics of a system and are easily computable. It would be interesting to follow the possibility to extend the here proposed approach to non-autonomous systems, such as the modulated neural networks processing cognitive stimuli.

#### ACKNOWLEDGMENTS

The authors acknowledge the financial support from the German research foundation (DFG). H.W. acknowledges the support from Stiftung Polytechnische

TABLE I. Short pseudo-code description how to compute the adiabatic fixed points (AFP) and target points.

<b>Computing AFP</b>
<ol style="list-style-type: none"> <li>1. Compute <math>\{\mathbf{x}(t_k), \mathbf{b}(t_k)\}_{0 \leq k \leq L}</math> as a solution of the ODE system (9), (10) at the time steps <math>t_k \in \{t_0, t_1, \dots, t_L\}</math> for any <math>\epsilon_b &gt; 0</math>.</li> <li>2. For every time step <math>t_k</math> do: <ol style="list-style-type: none"> <li>(a) Set <math>\mathbf{b} = \mathbf{b}(t_k)</math> in Eq. (10).</li> <li>(b) Repeat until you found all AFP: <ol style="list-style-type: none"> <li>(i) Minimize the kinetic energy <math>q_x</math> (3) starting from random <math>\mathbf{x}</math>.</li> <li>(ii) Check: If the kinetic energy at the local minimum is of the order of numerical accuracy (but at most <math>q_x \approx 10^{-12}</math>), then you found an AFP; else reject the point.</li> </ol> </li> </ol> </li> </ol>
<b>Computing target points</b>
<ol style="list-style-type: none"> <li>1. Compute <math>\{\mathbf{x}(t_k), \mathbf{b}(t_k)\}_{0 \leq k \leq L}</math> as a solution of the ODE system (10), (9) at the time steps <math>t_k \in \{t_0, t_1, \dots, t_L\}</math> for any <math>\epsilon_b &gt; 0</math>.</li> <li>2. For every time step <math>t_k</math> do: <ol style="list-style-type: none"> <li>(a) Solve the ODE (10) of the fast subsystem starting from <math>\{\mathbf{x}(t_k), \mathbf{b}(t_k)\}</math>, a point on the trajectory.</li> <li>(b) Check: If the solution converged <math>\dot{\mathbf{x}} \rightarrow 0</math>, you found the corresponding target point.</li> </ol> </li> </ol>

Gesellschaft Frankfurt am Main.

### Appendix A: Computing adiabatic fixed points and target points

For an alternative view we present in Table I a short pseudo-code description that explains, how to effectively compute AFP and target points. If more complex critical manifolds would be present, e. g. a limit cycle or a strange attractor, one could generalize the concept (2) to include these.

### Appendix B: Fixpoints of the three-neuron system

The six dimensional three-neuron system Eqs. (10), (9) has the only fixed point

$$x_2 = 1, \quad x_1 = x_3 = (1 + w_{13})/2, \quad b_i = x_i. \quad (\text{B1})$$

From that it follows that the neurons are half-active  $y_i = 1/2$  in the fixed point. This fixed point is generally stable for large values of  $\epsilon_b$ , undergoing a supercritical Hopf bifurcation when  $\epsilon_b$  becomes smaller. This occurs, for  $a = 6$  and  $w_{13} = -1$ , at  $\epsilon_b = 1/36 \approx 0.0278$ .

### Appendix C: Traveling waves

One can prove that in the case of symmetric coupling  $w_{13} = -1$  a traveling waves ansatz solves the system. This solution shows a relative phase shift of exactly  $\Delta_{13} = \frac{\tau}{3}$  between the first and the third neuron, where  $\tau$  is the period of the solution. We make an ansatz for the solution

$$\begin{aligned} x_1(t) &= x(t - \theta), & x_2(t) &= 1 + x(t), & x_3(t) &= x(t + \theta) \\ b_1(t) &= b(t - \theta), & b_2(t) &= 1 + b(t), & b_3(t) &= b(t + \theta) \end{aligned} \quad (\text{C1})$$

with two periodic functions  $x(t)$ ,  $b(t)$  of period  $\tau$  and an arbitrary shift  $\theta$ . The corresponding firing rates of the neurons therefore are given by

$$y_1(t) = y(t - \theta), \quad y_2(t) = y(t), \quad y_3(t) = y(t + \theta), \quad (\text{C2})$$

where the notation for the periodic function  $y(t) = y(x(t), a, b(t))$  is used. From this we get to the resulting equations of motion for the membrane potential

$$\begin{aligned} \dot{x}(t) &= -x(t) + y(t + \theta) - y(t + 2\theta) \\ \dot{x}(t) &= -x(t) + y(t - \theta) + y(t + \theta) - 1 \\ \dot{x}(t) &= -x(t) + y(t - \theta) - y(t - 2\theta). \end{aligned} \quad (\text{C3})$$

This leads to the condition  $y(t) = 1 - y(t \pm 3\theta)$  that has to hold when solving Eq. (C3). Assuming further that  $x(t + \frac{\tau}{2}) = -x(t)$  and  $b(t + \frac{\tau}{2}) = -b(t)$ , one can solve Eq. (C3) for the constant phase shift  $\theta = \frac{\tau}{6}$ . Therefore the phase shift  $\Delta_{13}$  between the first and the third neurons is exactly  $\Delta_{13} = 2\theta/\tau = 1/3$ .

[1] E. I. Moser, E. Kropff, and M.-B. Moser, Annual review of neuroscience **31** (2008).  
[2] J. J. Hopfield, Proceedings of the National Academy of Sciences **79**, 2554 (1982).  
[3] T. J. Wills, C. Lever, F. Cacucci, N. Burgess, and J. O'Keefe, Science **308**, 873 (2005).

[4] M. Rabinovich, R. Huerta, and G. Laurent, Science **321**, 48 (2008).  
[5] J. Niessing and R. W. Friedrich, Nature **465**, 47 (2010).  
[6] P. Miller and D. B. Katz, The Journal of Neuroscience **30**, 2559 (2010).  
[7] C. Gros, New Journal of Physics **9**, 109 (2007).

- [8] G. Deco and V. K. Jirsa, *The Journal of Neuroscience* **32**, 3366 (2012).
- [9] G. Deco, V. K. Jirsa, and A. R. McIntosh, *Nature Reviews Neuroscience* **12**, 43 (2011).
- [10] A. Zalesky, A. Fornito, L. Cocchi, L. L. Gollo, and M. Breakspear, *Proceedings of the National Academy of Sciences of the United States of America* **111**, 10341 (2014).
- [11] P. Ritter, V. K. Jirsa, A. R. McIntosh, and M. Breakspear, *Frontiers in Computational Neuroscience* **9**, 77 (2015).
- [12] L. Martin, B. Sándor, and C. Gros, *Frontiers in neuro-robotics* **10** (2016).
- [13] C. Gros and G. Kaczor, *Logic Journal of IGPL* **18**, 686 (2009).
- [14] C. Gros, *Cognitive Computation* **1**, 77 (2009).
- [15] M. Lukoševičius and H. Jaeger, *Computer Science Review* **3**, 127 (2009).
- [16] F. S. Neves and M. Timme, *Physical Review Letters* **109**, 018701 (2012).
- [17] H. Jaeger, German National Research Center for Information Technology GMD Technical Report **148**, 13 (2001).
- [18] N. Berglund and B. Gentz, *Noise-induced phenomena in slow-fast dynamical systems: a sample-paths approach* (Springer Science & Business Media, 2006).
- [19] C. Kuehn, *Multiple time scale dynamics*, Vol. 191 (Springer, 2015).
- [20] E. M. Izhikevich, *Dynamical systems in neuroscience* (MIT press, 2007).
- [21] F. Verhulst, *Nonlinear Dynamics* **50**, 747 (2007).
- [22] P. Szmolyan and M. Wechselberger, *Journal of Differential Equations* **200**, 69 (2004).
- [23] C. Gros, *Complex and Adaptive Dynamical Systems: A Primer* (Springer, 2015).
- [24] C. Rocsoreanu, A. Georgescu, and N. Giurgiteanu, *The FitzHugh-Nagumo model: bifurcation and dynamics*, Vol. 10 (Springer Science & Business Media, 2012).
- [25] Y. Zheng and L. Bao, *Communications in Nonlinear Science and Numerical Simulation* **19**, 1591 (2014).
- [26] F. Verhulst and T. Bakri, *Journal of the Indonesian Mathematical Society*, 1 (2006).
- [27] C. Kuehn, *Physical Review E* **85**, 026103 (2012).
- [28] C. Kuehn, *Journal of Physics A* **42**, 045101 (2008).
- [29] N. Berglund, *Progress of Theoretical Physics Supplement* **139**, 325 (2000).
- [30] S. J. Kiebel, J. Daunizeau, and K. J. Friston, *PLoS Comput Biol* **4**, e1000209 (2008).
- [31] C. Tetzlaff, C. Kolodziejcki, I. Markelic, and F. Wörgötter, *Biological Cybernetics* **106**, 715 (2012).
- [32] Y. Yamashita and J. Tani, *PLoS Comput Biol* **4**, e1000220 (2008).
- [33] M. Linkerhand and C. Gros, *Scientific Reports* **3** (2013).
- [34] C. Gros, M. Linkerhand, and V. Walther, in *Artificial Neural Networks and Machine Learning–ICANN 2014* (Springer, 2014) pp. 65–72.
- [35] D. Sussillo and O. Barak, *Neural Computation* **25**, 626 (2013).
- [36] D. Marković and C. Gros, *Neural Computation* **24**, 523 (2012).
- [37] E. Simonyi, *Periodica Polytechnica Electrical Engineering* **11**, 309 (1967).
- [38] E. N. Lorenz, *Journal of the atmospheric sciences* **49**, 2449 (1992).
- [39] D. Markovic and C. Gros, *Physical Review Letters* **105**, 068702 (2010).
- [40] M. Born and R. Oppenheimer, *Annalen der Physik* **389**, 457 (1927).
- [41] M. Franzius, N. Wilbert, and L. Wiskott, *Neural computation* **23**, 2289 (2011).
- [42] A. A. Prinz, D. Bucher, and E. Marder, *Nature Neuroscience* **7**, 1345 (2004).
- [43] J. P. Miller and A. I. Selverston, *Journal of Neurophysiology* **48**, 1416 (1982).
- [44] R. J. Morgan and I. Soltesz, *Proceedings of the National Academy of Sciences* **105**, 6179 (2008).
- [45] J. Triesch, in *Artificial Neural Networks: Biological Inspirations–ICANN 2005* (Springer, 2005) pp. 65–70.
- [46] E. Fehlberg, *NASA Technical Report* **315** (1969).
- [47] C. G. Broyden, *IMA Journal of Applied Mathematics* **6**, 76 (1970).
- [48] D. F. Shanno, *Mathematics of Computation* **24**, 647 (1970).
- [49] “dlib C++ optimization library,” <http://dlib.net/optimization.html>, accessed: 08.02.2016.
- [50] F. Pollmann, E. Berg, A. M. Turner, and M. Oshikawa, *Physical review b* **85**, 075125 (2012).
- [51] J. Guckenheimer and P. Holmes, *Nonlinear oscillations, dynamical systems, and bifurcations of vector fields*, Vol. 42 (Springer Science & Business Media, 2013).
- [52] H. Wernecke, B. Sándor, and C. Gros, *Scientific Reports* **7** (2017).
- [53] T. Tél and M. Gruiz, *Chaotic Dynamics: An Introduction Based on Classical Mechanics* (Cambridge University Press, 2006) p. 393.